Occurrence of sand boils landside of a river dike during flooding: A geophysical perspective

A Ghorbani, André Revil, S Bonelli, S Barde-Cabusson, L Girolami, F Nicoleau, P Vaudelet

Engineering Geology 329 (2024) 107403

Contents lists available at ScienceDirect

Engineering Geology

journal homepage: www.elsevier.com/locate/enggeo

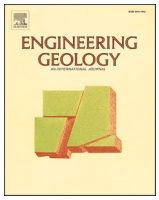

Occurrence of sand boils landside of a river dike during flooding: A geophysical perspective

A. Ghorbani [a], A. Revil [b,*], S. Bonelli [c], S. Barde-Cabusson [a,d], L. Girolami [c,e], F. Nicoleau [f], P. Vaudelet [a]

[a] Naga Geophysics, Technolac, 73370 Le Bourget du Lac, France
[b] Université Grenoble Alpes, Univ. Savoie Mont-Blanc, CNRS, UMR CNRS 5204, EDYTEM, 73370 Le Bourget du Lac, France
[c] INRAE Aix-Marseille Université UMR RECOVER, Aix-en-Provence 13100, France
[d] Geosciences Barcelona (GEO3BCN), CSIC, Lluís Solé Sabarís s/n, 08028 Barcelona, Spain
[e] GéHCO, Campus Grandmont, Université de Tours, 37200 Tours, France
[f] Syndicat Mixte du Bassin Versant de l'Agly, 16 Rue de Lesquerde, Saint-Paul-de-Fenouillet, France

ARTICLE INFO

Keywords:
Induced polarization
Embankment
Leakage
Sand boil
Resistivity
Chargeability
Liquefaction

ABSTRACT

The study of internal erosion of earth dams, dikes, and levees is an essential ingredient to address their safety. Indeed, internal erosion is known to be a major cause of failure for dams and levees. Several sections of the Agly river dike (south-west France) are affected by the appearance of sand boils on the side of the protected zone. These phenomena generally occur without any significant erosion of the dike itself. In order to better understand the reasons for these phenomena, we took advantage of a drought (dry riverbed) to image, using induced polarization tomography, the subsurface from the riverbed to the plains extending inland behind the areas prone to these pathologies. Induced polarization imaging is a geophysical technique that extends the classical electrical resistivity tomography to include low-frequency polarization mechanisms. This approach shows that the river dike is partly built on a sand-filled paleochannel, allowing water to flow under the dike and its clay core during river floods. During floods, underground flow under the dike is responsible for sand boil phenomena on the side of the protected zone. Numerical hydraulic simulations show that the discharge zone has specific concentration points, particularly at the toe of the dike even when the permeability of the sand filling the paleochannel is homogeneous. These concentrated discharges are controlled by the water level in the river, the geometry of the dike and the shape of the clay-sand interface of the paleochannel. This study highlights the role of geophysical techniques, especially induced polarization, in providing key information to better understand erosion and fluidization phenomena affecting river dikes.

1. Introduction

Sand boils look like small mud volcanoes (Revil, 2002; Aloisi et al., 2004) formed by the outflow of sand onto the ground surface from a central crater landward a river dike, (Stephens, 2014, Fig. 1). They occur when the water level in the river is high (flooding conditions, see Robbins et al., 2019). They can range in size from few centimeters to several meters in diameter. Sometimes soil depression in the form of diatremes can be also observed (Figs. 1 and 2). These processes are associated with the partial fluidization of soils and can potentially contribute to dike failure during river floods (Fig. 1). The fluidization mechanism is attributed to the hydraulic head gradient on two sides of the embankment, levee or dike during a river flood when the pore water velocity exceeds a threshold value above which the drag balances the sandy particles weight which are locally fluidized and suspended into the outflows (Amin et al., 2021). It can lead to internal erosion and piping in the dike and its foundation (Bonelli, 2012; Bonelli, 2013; Van Beek et al., 2015). The formations of background erosion and piping can ultimately result in embankment failure (Robbins and Van Beek, 2015). Sometimes things can be trickier. Indeed, internal erosion can lead to subsidence of the river dike. Then during flooding, this subsidence can yield overflow from the river triggering in turn rapid erosion of the earthen dike from

* Corresponding author.
E-mail addresses: ahmad.ghorbani@naga-geophysics.com (A. Ghorbani), andre.revil@univ-smb.fr (A. Revil), stephane.bonelli@inrae.fr (S. Bonelli), laurence.girolami@inrae.fr (L. Girolami), pierre.vaudelet@naga-geophysics.com (P. Vaudelet).

https://doi.org/10.1016/j.enggeo.2024.107403
Received 14 July 2023; Received in revised form 3 December 2023; Accepted 2 January 2024
Available online 5 January 2024

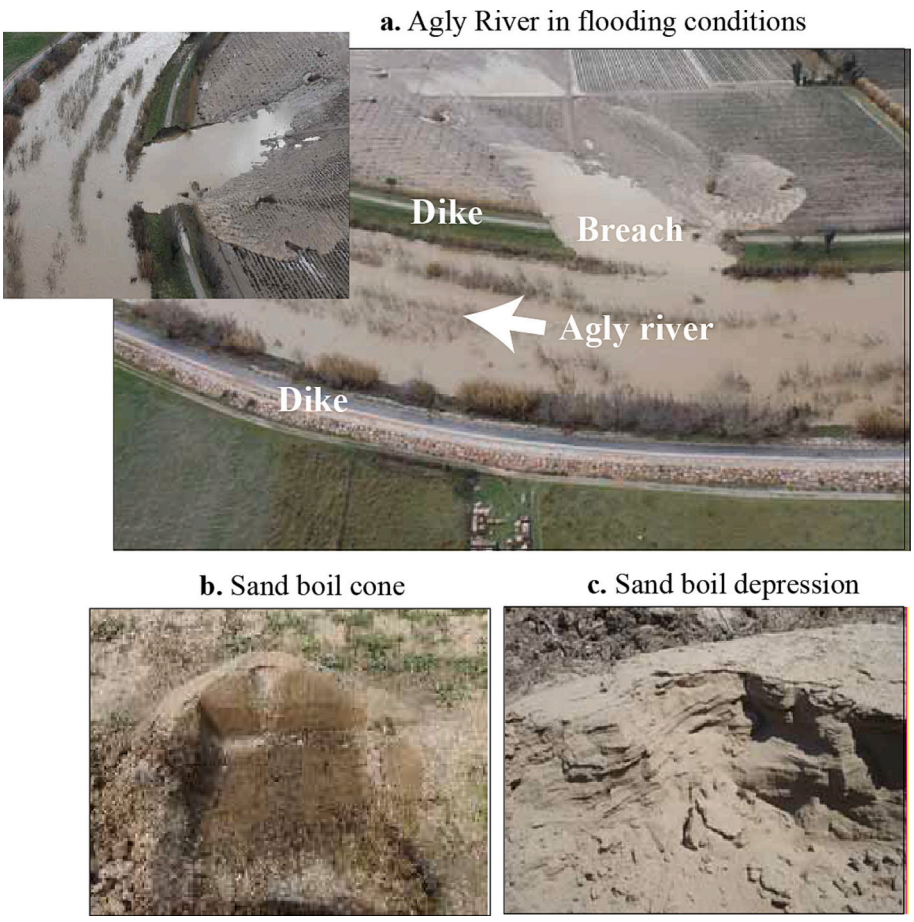

Fig. 1. Agly river. **a.** Flood conditions with overflow of the river over the river dike (the Pia breach, Event: March 6th, 2013). **b.** Sand boil in the form of a small mud volcano. **c.** Sand boil in the form of a diatreme. Source of the pictures: Civil Protection, Maurin and Ledoux, 2013).

above, and failure.

Agly is a 82 km-long river located in Southern France starting in the Corbières hills and flowing down to the Mediterranean Sea near the city of *Le* Barbarés (Fig. 2). The river is known for its strong floods recently enforced by extreme rain events associated with climate change. The large karst system of the Corbières hills can, in some occasions, amplify the floods of the Agly River (Carozza et al., 2013; Fleury et al., 2020). These floods are responsible for a number of observed fluidization phenomena along the banks of the river dikes including sand boils and subsidence phenomena landside the dike (Carozza et al., 2013). Note that the dikes of the Agly River are made of rammed earth materials locally reinforced with stone cladding and in some places with impervious geotextiles (Maurin and Ledoux, 2013).

Unintended seepage paths in earth dams, dikes, and levees are generally caused by backward erosion phenomena. They present serious threats to their integrity as reviewed by Fell et al. (1992, 2003) and lead to their collapse. Therefore, the detection, delineation and continuous monitoring of such seepages is of paramount importance in any adequate and appropriate maintenance task. Various geophysical methods can be used to study dams, enbankments, and levees and can be combined to increase their efficiency (e.g., Himi et al., 2018).

The self-potential method is able to localize seepages in earth dams, dikes and levees (Panthulu et al., 2001; Bolève et al., 2007, 2009). Ground Penetrating Radar (GPR) constitutes a fast and reliable method for shallow investigations. However, the so-called skin-depth of GPR (i.e., the depth of penetration of the electromagnetic waves at a given frequency) can be very small in conductive media, for instance in presence of clays (Antoine et al., 2015) and is therefore not often used in the study of earth dams and levees.

Electrical conductivity do not suffer such a limitation and is known to provide important information for the assessment of preferential flow paths (e.g., Perri et al., 2014; Fargier et al., 2014; Johansson and Dahlin, 1996) and can be efficiently associated with seismic methods (e.g., Cardarelli et al., 2014). However electrical conductivity tomography can be hardly used as a stand-alone technique. Indeed, two contributions control the electrical conductivity of porous media, one associated with bulk conduction and the second obe with surface conduction on the surface of the grains. These two contribution have different dependence to the water content.

Induced polarization is a geophysical method able to non-intrusively image the geoelectrical properties of soils, sediments, and rocks with a unique sensitivity to their hydraulic properties (Schlumberger, 1920; Vinegar and Waxman, 1984; Nordsiek et al., 2015; Revil et al., 2020). It is an extension of the electrical resistivity method mentioned above (e.g., Hauck, 2002) and is commonly performed with the same equipment to address environmental issues in hydrogeophysics (see Binley et al., 2015, and references therein). Induced polarization refers to the use of low-frequency polarization mechanisms in porous bodies, typically occurring in the frequency range 1 mHz to 10 kHz (Vinegar and Waxman, 1984; Zimmermann et al., 2008; Günther and Martin, 2016). This method is sensitive to grain and pore sizes, permeability, and electrochemical interactions at the surface of the grains (Revil and Florsch, 2010; Vaudelet et al., 2011; Revil et al., 2014).

For a long-time, induced polarization was underused in environmental geosciences because of a lack of understanding of the underlying physics. The underlying mechanisms of conduction and polarization are now better understood in sands, sandstones, and clay-rich materials (Zisser and Nover, 2009; Zisser et al., 2010; Jougnot et al., 2010; Weller

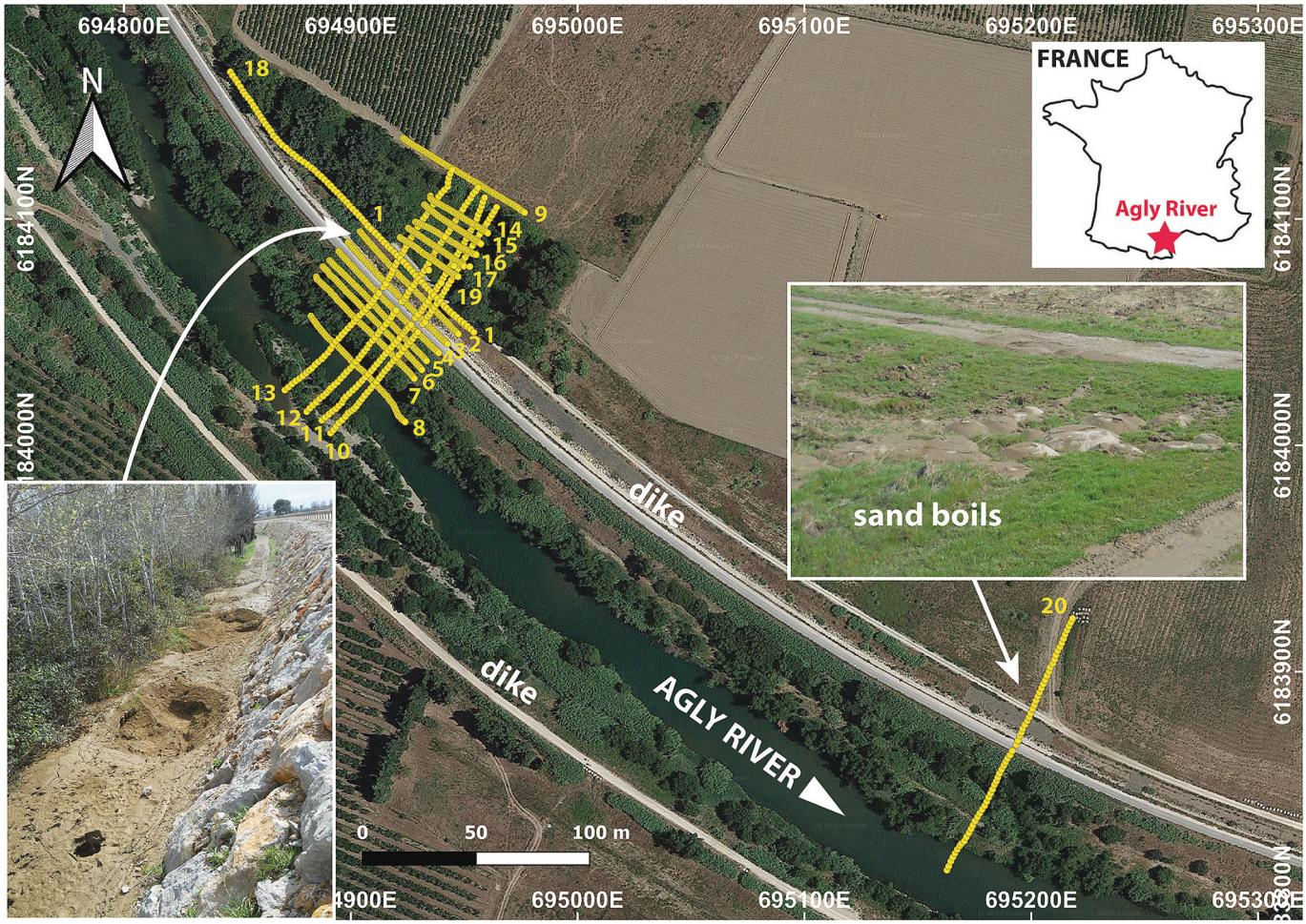

Fig. 2. The Agly River is located in the South-West of France and is known for its strong floods. In Spring 2023, we performed 20 induced polarization profiles representing 7962 measurements and 1136 electrodes marked by the yellow dots. 2.5D and 3D inversions were performed to obtain tomograms of the resistivity and normalized chargeability. Seepage behavior during floods reveals large sand boils landward with respect to the position of the dikes (as shown on the pictures) with significant erosion without dike breaches. The river dikes are underlined by the roads parallel to the two sides of the river banks. (For interpretation of the references to colour in this figure legend, the reader is referred to the web version of this article.)

et al., 2013; Revil, 2013a, 2013b; Abdulsamad et al., 2023) including in geoengineering problems (see El Alam and Revil, 2023, and references therein). In absence of metallic grains, the underlying physics is associated with the polarization of the electrical double layer coating the surface of the grains (Revil, 2013a, 2013b; Niu et al., 2016, see Fig. 3).

In the field, we use multielectrode systems connected to a resistivity meter. During the injection of an electrical current between two electrodes A and B, we measure the resulting voltage between two other electrodes M and N providing an apparent resistivity value using Ohm's law (Fig. 3). After shutting down the primary current, we measure the secondary voltage decay between two other electrodes M and N (Schlumberger, 1920; see Fig. 3). A porous material can be considered as an equivalent circuit with a resistance in parallel with a resistance and a capacitance (Vinegar and Waxman, 1984; Revil et al., 2017). The secondary voltage decay is associated with the electrical charge reversibly stored in the capacitance over time (i.e., in the polarization of the electrical double layer around the grains, Revil et al., 2017).

A geophysical survey was undertaken in March 2023 to elucidate the reasons for the presence of sand boils and erosion phenomena on parts of the Agly river dike (Fig. 2). Our goal was to understand the reasons for the existence of these features through geophysical observations and hydrogeological modeling without undertaking, at least in the present paper, the difficult task of hydromechanical modeling and non-linear flow mechanism associated with shock/solitary waves.

2. Geophysical survey

2.1. Position of the problem

The Agly River is known for fast flooding events like the one shown in Fig. 1. In the period of high water levels, there are some portions of the dike bordering the river that exhibit fluidization phenomena as shown in Figs. 1 and 2. A geophysical survey was carried out in Spring 2023 to better understand the properties of the subsurface and the lithofacies able to control seepage and the occurrence of these phenomena.

Induced polarization is a geophysical method that is an extension of the electrical resistivity method broadly used in environmental geosciences. It can be carried out with the same equipment than used for a resistivity survey and inside the same time frame. In the last decade, a petrophysical model called the dynamic Stern layer model has been developed (Revil, 2013a, 2013b, see also Chew and Sen, 1982a, 1982b) and checked with large experimental datasets (e.g., Revil et al., 2017). This model has also been applied in field conditions to study landslides (Revil et al., 2020), permafrost (Duvillard et al., 2018; Wagner et al., 2019), or leakages in dikes and embankments (Abdulsamad et al., 2019). This model is summarized in Section 2.2 and applied to interpret geophysical data in Section 3 below.

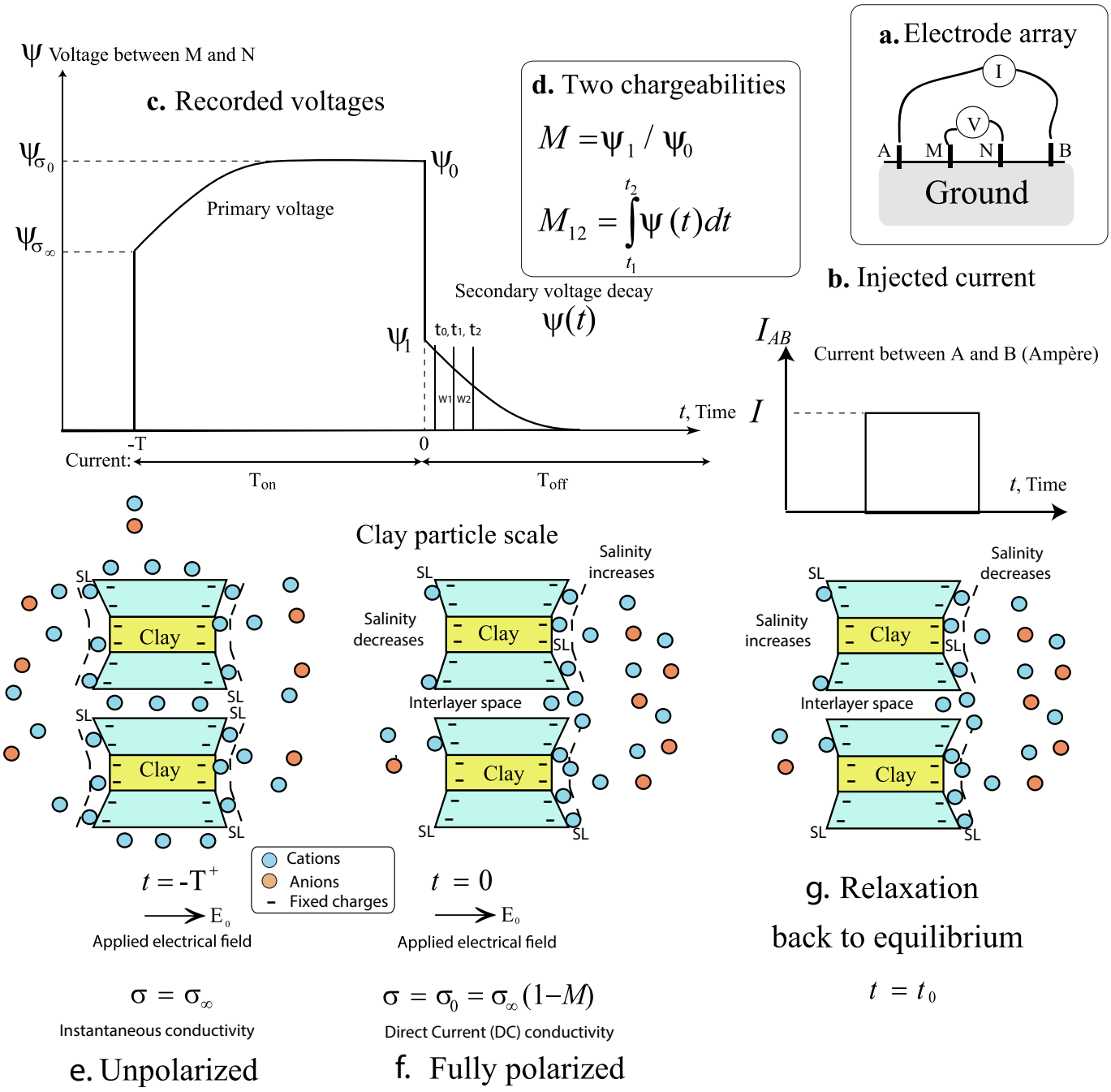

Fig. 3. Time-domain induced polarization. **a.** Electrode array: AB current electrodes, MN voltage electrodes. **b.** Current box $I(t)$ (in A) applied over time (during T_{on}) at AB. **c.** Voltage difference between M and N recorded over time. **d.** Definitions of the partial (apparent chargeabilities) in ms and in mV/V through a set of time windows w_i. **e.** At the particle scale, sketch of the electrical charge distribution just after the application of the current I. **f.** Charge distribution at the end of the application of the current. **g.** Charge distribution going back to equilibrium by electro-diffusion in the concentration gradient created by the application of the applied current or electrical field. $\mathbf{E}_0$ corresponds to the primary electrical field.

2.2. The dynamic Stern layer model

In time-domain induced polarization, a sketch of the imposed current and voltage time series is shown in Fig. 3 as well as the polarization and depolarization of a clay particle during the process. The Stern layer corresponds to the inner part of the electrical double layer coating the surface of the mineral grains. According to Zukoski and Saville (1986a, 1986b), this layer should be treated in a dynamic sense. When an electrical field is applied to a clay particle, all the charges around the clay particle can move through electromigration. Then some of the positive charges accumulate in the direction of the electrical field letting a negative charge behind on the mineral surface. The clay particle behaves as a giant dipole. The electrical conductivity in this DC (Direct Current) situation is smaller than the instantaneous conductivity (just after the application of the electrical field) since the charges associated with polarization are not available anymore for conduction. When the primary electrical field is shut down, the accumulated electric charges are coming back to their equilibrium position (Fig. 3g). The ion transport around the clay particle is described by the Nernst-Planck equation involving both diffusion and electromigration along the mineral surface

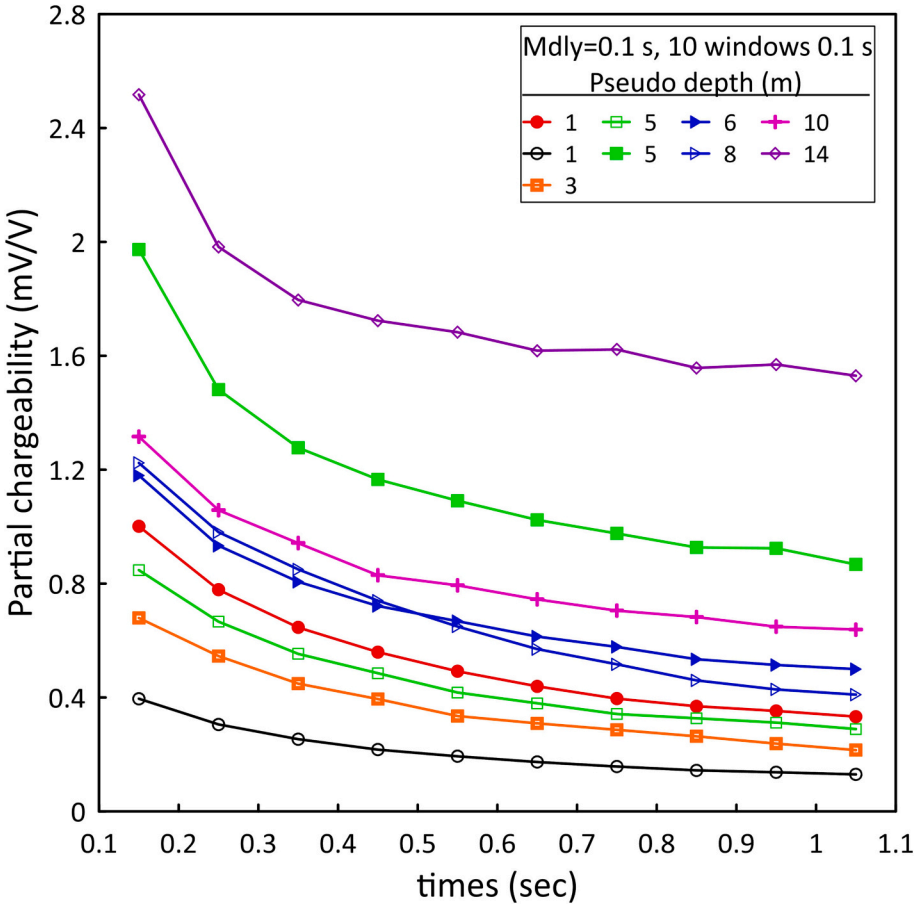

Fig. 4. Example of decay curves shown in terms of partial chargeability (here expressed in mV/V) versus the elaspsed time after shutting down the primary current. We use a primary current injection duration of 1 s and the decay curves are measured using ten windows of 0.1 s after a dead time of 0.1 s. The induced polarization data are shown here for pseudo-depths ranging from 1 m to 14 m and underlines the high quality of the signals.

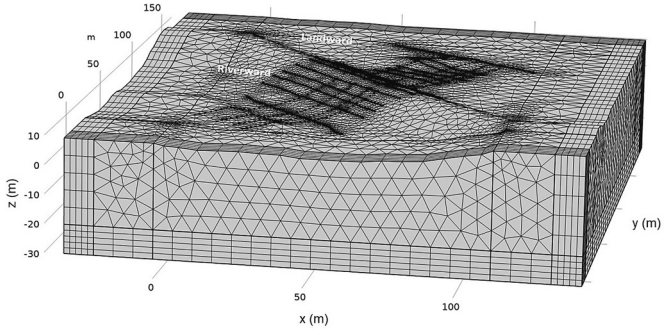

Fig. 5. Mesh used for the forward and inverse models for the area covered by Profiles 1 to 19 (see Fig. 1). The mesh comprises a total of 17,125 elements and is refined close to the 1136 electrodes. The topography of the side is taken from a Digital Elevation Map (DEM) with a precision of 20 cm.

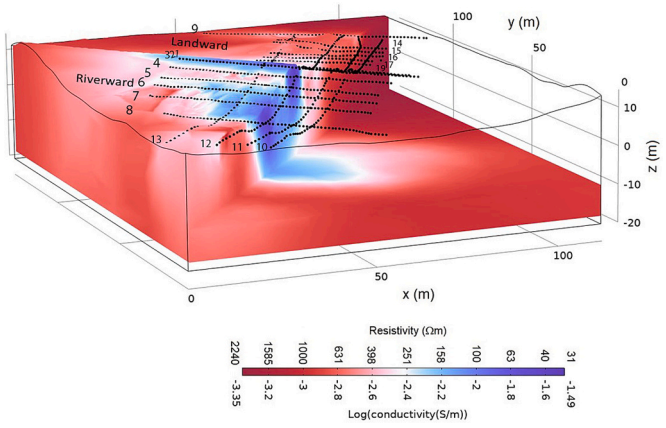

Fig. 6. 3D electrical resistivity tomogram at the 5th iteration. The tomogram exhibits a resistive body (resistivity in the range 30–300 Ohm m) below the river dike corresponding to a sand-rich body likely associated with a paleo-channel of the river. In case of flooding, this water-bearing sand body is serving as unconfined aquifer (RMSE 0.1943).

(de Lima and Sharma, 1992).

The (instantaneous) electrical conductivity σ_∞ is a macroscopic physical property characterizing the ability of a porous material to let the current pass through it. It corresponds to the conductivity just after the application of the current between the electrodes A and B (Fig. 3a,b, c,d). The normalized chargeability $M_n = M\,\sigma_\infty$ (M denotes the chargeability) describes the ability of the same material to store reversibly electrical charges during the passage of a primary current.

Archie (1942) proposed an electrical conductivity model for clay-free sandstones accounting for the conduction along the connected pore space partially or fully-saturated by an electrolyte. Waxman and Smits (1968) developed a model describing the conductivity of siliclastic sediments in order to interpret downhole measurements in oil fields. They included the so-called surface conductivity corresponding to the electromigration of the ions along the electrical double layer surrounding the minerals. Later, Vinegar and Waxman (1984) extended the

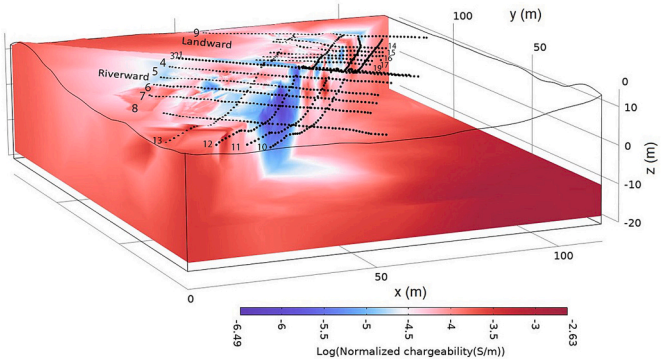

Fig. 7. 3D normalized chargeability tomogram at iteration at the 5th iteration. The tomogram exhibits a low polarizable body (normalized chargeability in the range 10^{-5} to $10^{-6.5}$ S m^{-1}) below the dike confirming the existence of a sand-rich body likely associated with a paleochannel of the river (RMSE for the chargeability 0.1943).

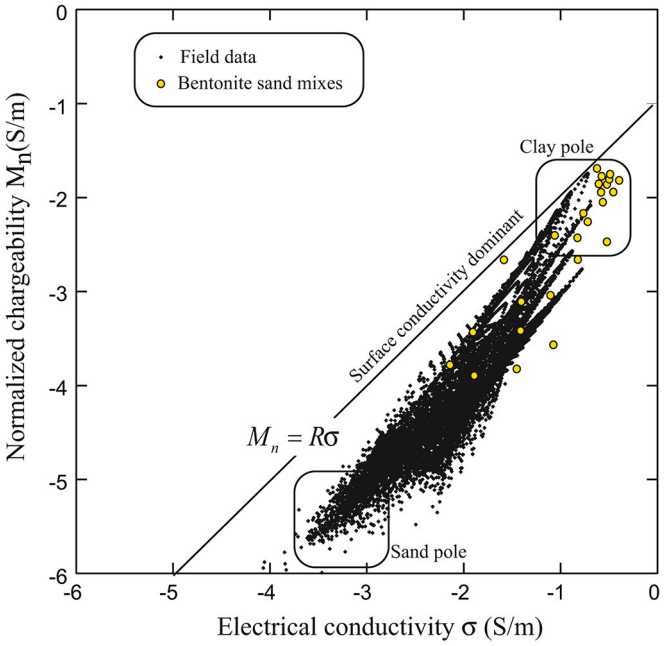

Fig. 8. Normalized chargeability versus electrical conductivity. The data exhibit two poles, one characterized by high surface conductivity (when the ratio between the normalized chargeability and the conductivity is equal to the dimensionless number R) and a sandy pole for which the conductivity is dominated by the bulk conductivity. Sand is characterized by relatively high resistivity (low conductivity) and low normalized chargeability. The yellow filled circles correspond to laboratory data for bentonite sand mixtures similar to the smectite-sand mixes observed in the field. (For interpretation of the references to colour in this figure legend, the reader is referred to the web version of this article.)

WS model to include the low-frequency polarization of the electrical double layer coating the surface of the mineral grains and especially the inner part of the electrical double layer call the Stern layer (see Zukoski and Saville, 1986a, 1986b). When a soil is partially saturated with ground water, Revil (2013a, 2013b) and Revil et al. (2017) obtained the following expressions for the electrical conductivity σ_∞ (in S m^{-1}) and normalized chargeability M_n (both in S m^{-1})

$$\sigma_\infty = \theta^m \sigma_w + \theta^{m-1} \rho_g B \, \mathrm{CEC} \tag{1}$$

$$M_n = \theta^{m-1} \rho_g \lambda \, \mathrm{CEC} \tag{2}$$

where ρ_g corresponds to the grain density (typically 2650 ± 100 kg m^{-3} for siliciclastic sediments) and CEC denotes the Cation Exchange Capacity of the sediment (expressed in C kg^{-1} or alternatively in meq/100 g with 1 cmol/kg = 1 meq/100 g = 963.20C kg^{-1} in SI units). The CEC is broadly used quantity in agronomy to characterize the quality of soils. The CEC of a siliciclastic sediment is mostly controlled by the types and amount of clays that are present (Waxman and Smits, 1968). The quantity σ_w denotes the pore water conductivity (proportional to the salinity and the temperature) while $m \approx 2.0 \pm 0.5$ denotes the porosity (cementation) exponent in Archie's law (Archie, 1942). We have assumed above that the saturation and porosity exponent have the same value. Finally, θ corresponds to the (volumetric) water content (volume of water over the volume of material) of the material (equal to the porosity in saturated conditions). The normalized chargeability of sand is known to be much smaller than the normalized chargeability of clay-rich materials, especially when smectite is present (Revil et al., 2013; Okay et al., 2014).

Coming back to Eqs. (1) and (2), the quantity B (in m^{2}s^{-1} V^{-1}) denotes the mobility of the counterions for conduction in the electrical double layer coating the surface of the grains, while λ (in m^{2}s^{-1} V^{-1}) denotes the mobility of the counterions for the polarization. A dimensionless number R was introduced by Revil et al. (2017) as $R = \lambda/B$. From Ghorbani et al. (2018), we have $B(Na^+, 25\,°C) = 3.1 \pm 0.3 \times 10^{-9}$ m^{2}s^{-1} V^{-1} and $\lambda(Na^+, 25\,°C) = 3.0 \pm 0.7 \times 10^{-10}$ m^{2}s^{-1} V^{-1}, and therefore $R \approx 0.10 \pm 0.02$.

When the conductivity of the pore water is known (i.e., the value of σ_w), Eqs. (1) and (2) are two equations with two unknowns θ and CEC (the values of the other parameters are rather well-established, see Revil et al., 2017). Then, cell-by-cell in the tomograms, we can determine the value of the water content and CEC from the value of the conductivity and normalized chargeability.

2.3. Geophysical survey

We use time-domain induced polarization for the field survey (Titov et al., 2002). We performed 2D acquisitions along 20 profiles in four days. Each profile is composed of 64 stainless steel electrodes with a spacing between the electrodes of 1 or 2 m. The acquisition is done with an ABEM-SAS4000 and the Wenner-alpha array with 472 measurements per profile. We performed a single stack per measurement in order to avoid dealing with the superposition principle in the electrical potential data recorded at the electrodes bipoles MN. Indeed, the secondary voltage takes a long time to fully relax. Therefore stacking produces results that are less and less repeatable. In our case, data quality is assessed based on the pseudo-section. Indeed, at each pseudo-depth, the pseudo-section is expected to be smooth and this is the case for our pseudo-sections. Outliers are removed in order to filter the data.

The Wenner-alpha array was selected for its good signal-to-noise ratio compared to other arrays (like the dipole dipole array) and because we can use the pseudo-section to filter out spurious data points (which is not easily the case with the multi-gradient array). The complete survey comprises 1136 electrodes and 7962 apparent resistivity and chargeability data. Some of the electrodes have been installed in the riverbed itself (Fig. 1), which was partly dry at the time of the survey.

The primary current is injected for a period of 1 s with a magnitude comprised between 20 and 200 mA. The contact resistances between the electrodes and the ground can be an issue in induced polarization (Ingeman-Nielsen, 2006). In our case, salty water was added to the electrodes to decrease the contact resistances below 1 kΩ. The secondary voltages are measured using 10 windows of 0.1 s with a dead time of 0.1 s. Some examples of the decay curves are shown in Fig. 4. We found that the data quality is high with few data removed from the apparent resistivity and apparent chargeability pseudo-sections.

The mesh used to do the 3D inversion is shown in Fig. 5. The mesh is created so we can apply a zero potential at infinity. The inversion is done

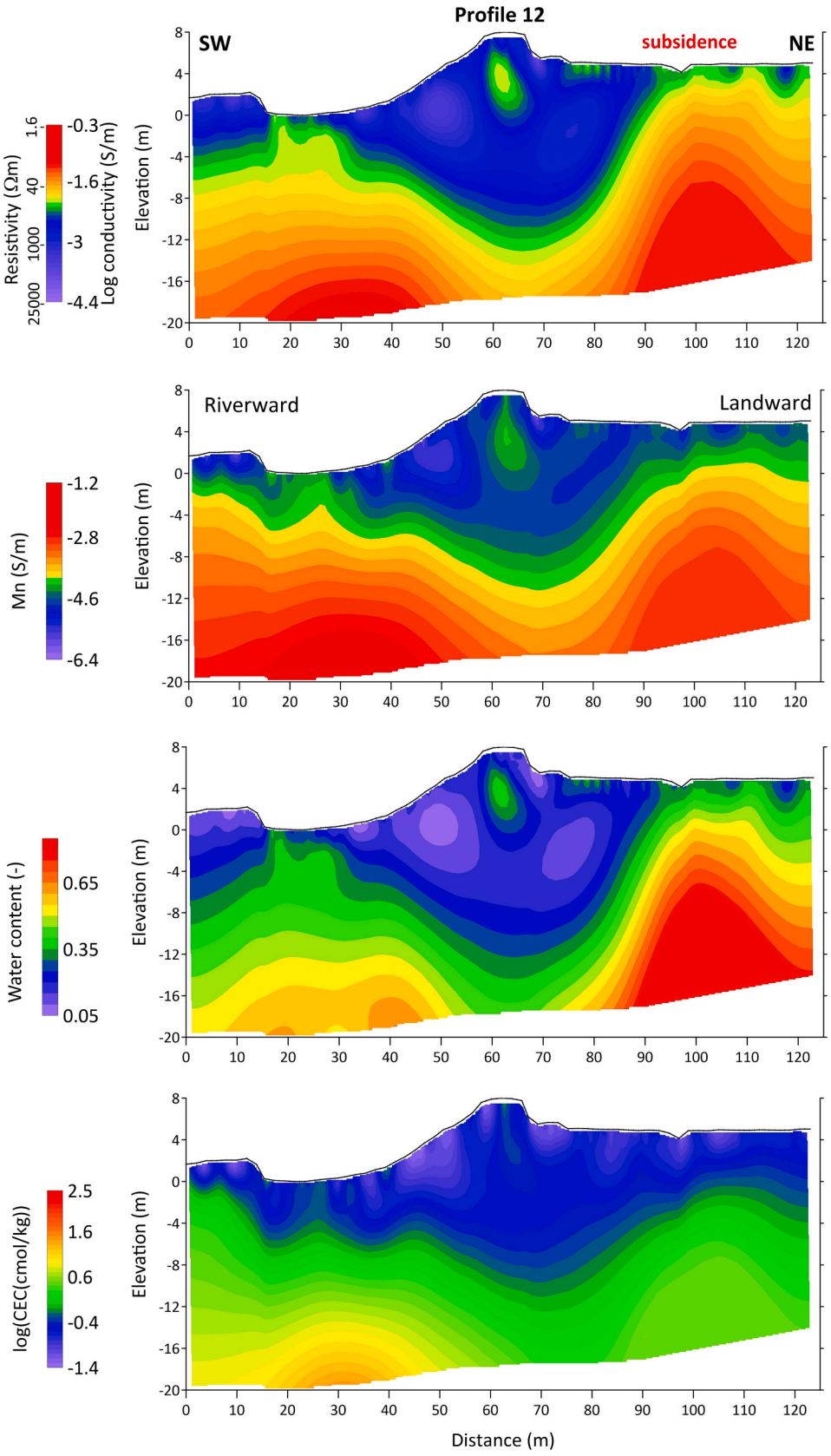

Fig. 9. Electrical conductivity, normalized chargeability, water content and cation exchange capacity tomograms for Profile 12 (see position in Fig. 2). The water content and the cation exchange capacity (1 cmol/kg = 1 meq/100 g) are obtained from the conductivity and the normalized chargeability using the dynamic Stern layer model discussed in the main test. Note that the water content in the sand layer is low because the measurements were taken during a drought.

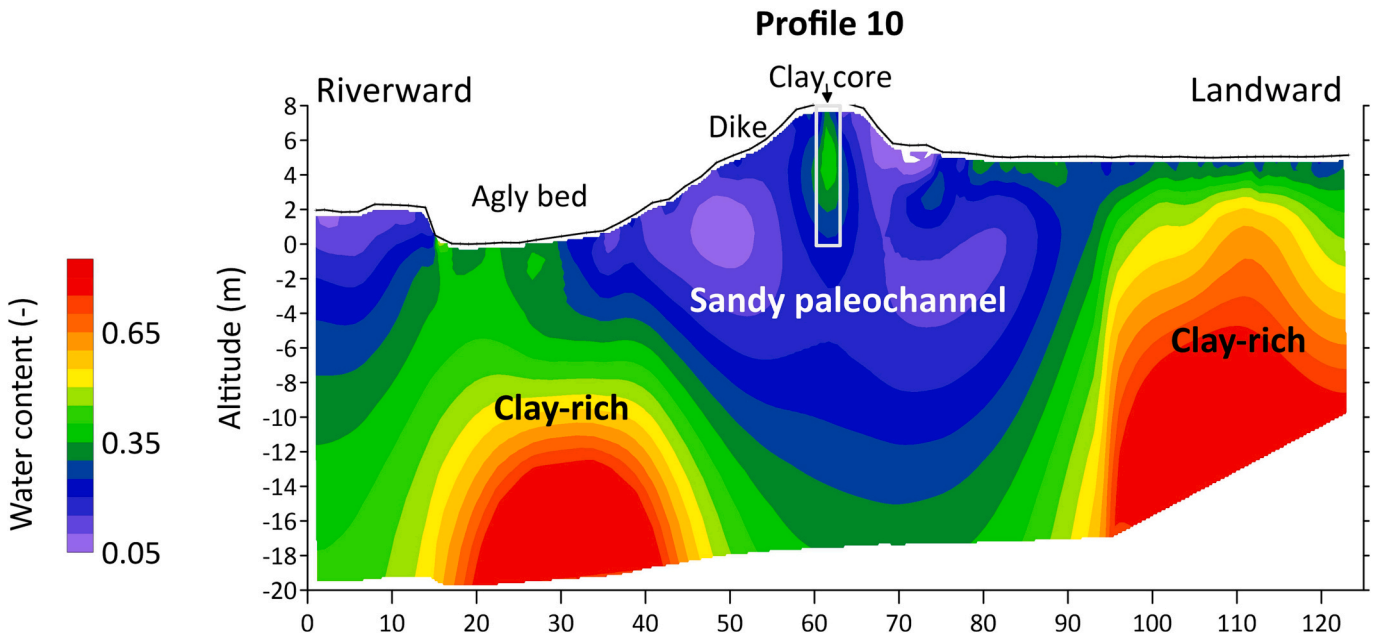

Fig. 10. Water content tomogram of Profile 10 (see position in Fig. 2). We can observe the clay core in the river dike. The depth of the paleochannel is roughly 15 m below the river bed. We observe that the clay core roughly extends down to the level of the river bed.

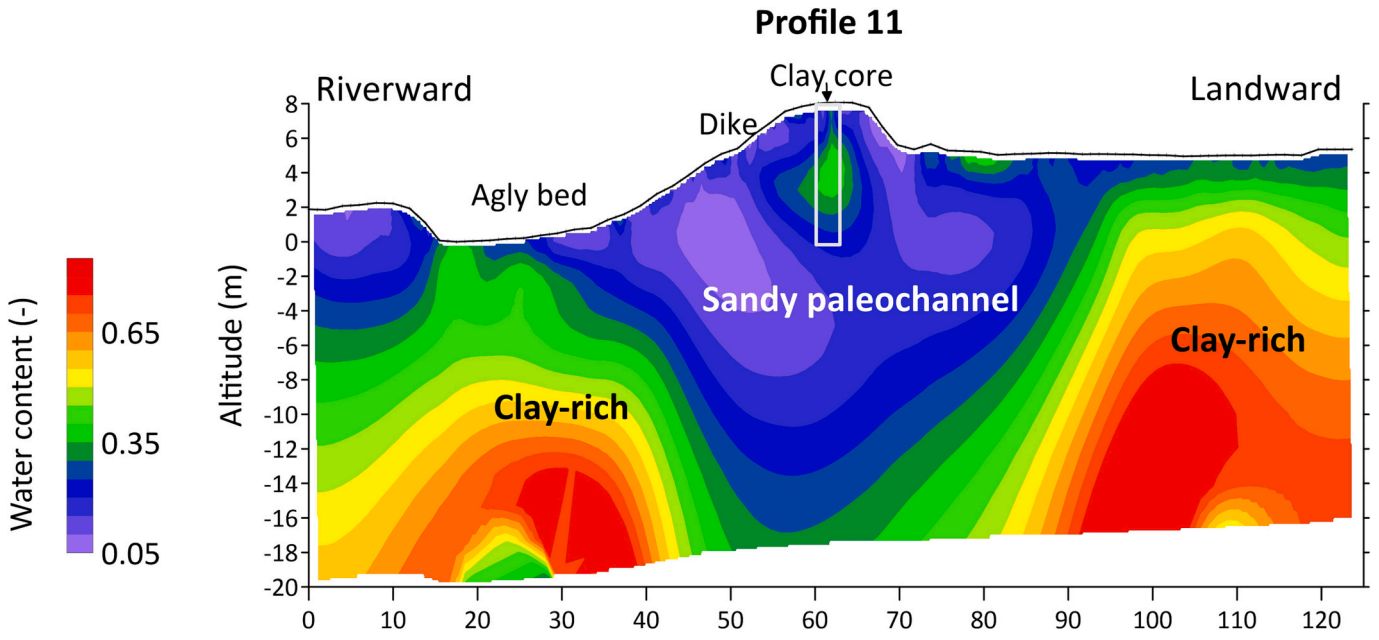

Fig. 11. Water content tomogram of Profile 11 (see position in Fig. 2). We can observe the clay core in the river dike. The depth of the paleochannel is roughly 16 m below the river bed and is dug into a clayey formation.

with a Gauss-Newton algorithm and convergence is reached at the 5th iteration using the code developed by Soueid Ahmed et al. (2018). The calculations are performed with an Intel Xeon Workstation (CPU E5–2683(x2), RAM memory 128Gb) and take 3 days. Once the apparent resistivity has been inverted, we do the same for the apparent chargeability data using the first time window in the decay curves shown in Fig. 4 (between 0.1 and 0.2 s) to obtain the apparent chargeability data. Once the chargeability is obtained through inversion, we get the normalized chargeability (in S m^{-1}) by taking the product between the conductivity and the chargeability. The same is done for the 2D profiles with a 2.5D inversion algorithm using RES2DINV (i.e., the earth model is assumed to be the same in the strike direction normal to the profile). Therefore the 2.5D inversion is particularly well-suited for the profiles normal to the river dike.

3. Results and interpretation

The 3D conductivity and normalized chargeability distributions are shown in Figs. 6 and 7, respectively. They show a resistive (low-conductivity) poorly chargeable body located below the dike and corresponding to a sand body. This body corresponds to a paleochannel filled with sand (actually sandy loam according to trenches and wells done in the area) and incised into a silty clay material. The situation is similar to the case study shown for instance by Revil et al. (2005) for a

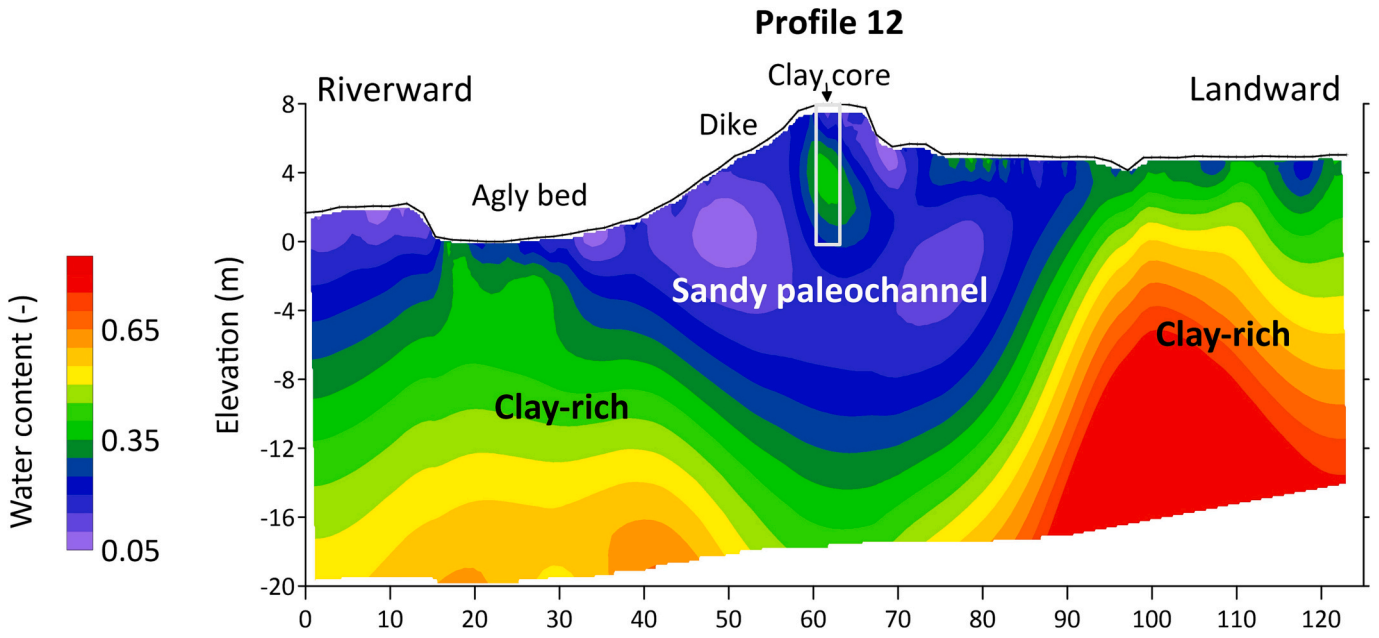

Fig. 12. Water content tomogram of Profile 12 (see position in Fig. 2). We can observe the clay core in the river dike. The depth of the paleochannel is roughly 13 m. We observe that the clay core roughly extends down to the level of the river bed.

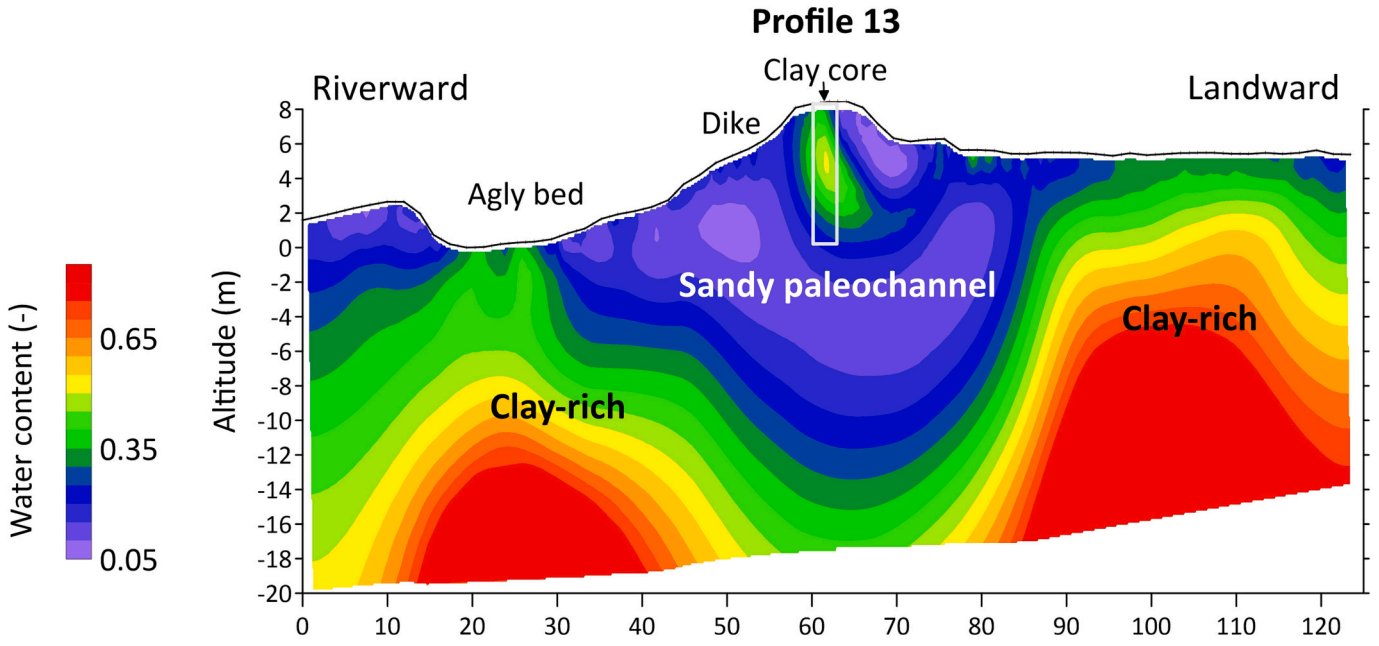

Fig. 13. Water content tomogram of Profile 13 (see position in Fig. 2). We can observe the clay core in the river dike. The depth of the paleochannel is roughly 14 m. We observe that the clay core extends down to the level of the river bed.

paleochannel of the Rhône river. The normalized chargeability data (for each element of the tomogram where there is enough sensitivity) is plotted as a function of the conductivity in Fig. 8. We see two poles: a clayey pole characterized by high values of the normalized chargeability and conductivity with a ratio close to R. For this pole, surface conductivity $\sigma_S \equiv \theta^{m-1}\rho_g B\mathrm{CEC}$ dominates therefore the conductivity response. The second pole is characterized by low values of the normalized chargeability and conductivity. It corresponds to the sandy pole. For this pole, the ratio between the two quantities is far from the line $M_n = R\,\sigma$. This means that the conductivity is dominated by its bulk component $\theta^m\sigma_w$.

The conductivity of the ground water σ_w was sampled in the field and measured in the laboratory measured. We obtained 700 μS cm^{-1} at 25 °C. Using the dynamic Stern layer model described above, we can determine the water content and CEC of the subsurface. A complete example is shown in Fig. 9. The paleochannel is characterized by small CEC values (~0.1–1 meq/100 g) while the background material is characterized by higher CEC values (~10 meq/100 g) associated with the presence of clays. VBS (methylene blue test, Carter et al., 1965) measurements have been performed on 17 samples from the site and the CEC values are 0.1 and 2 meq/100 g (using the conversion formula CEC (meq/100 g) = VB(g/100 g)/M with M = 319.8 g/mol being the molecular mass of methylene Blue). VBS has a tendency to underestimate the CEC in presence of smectite.

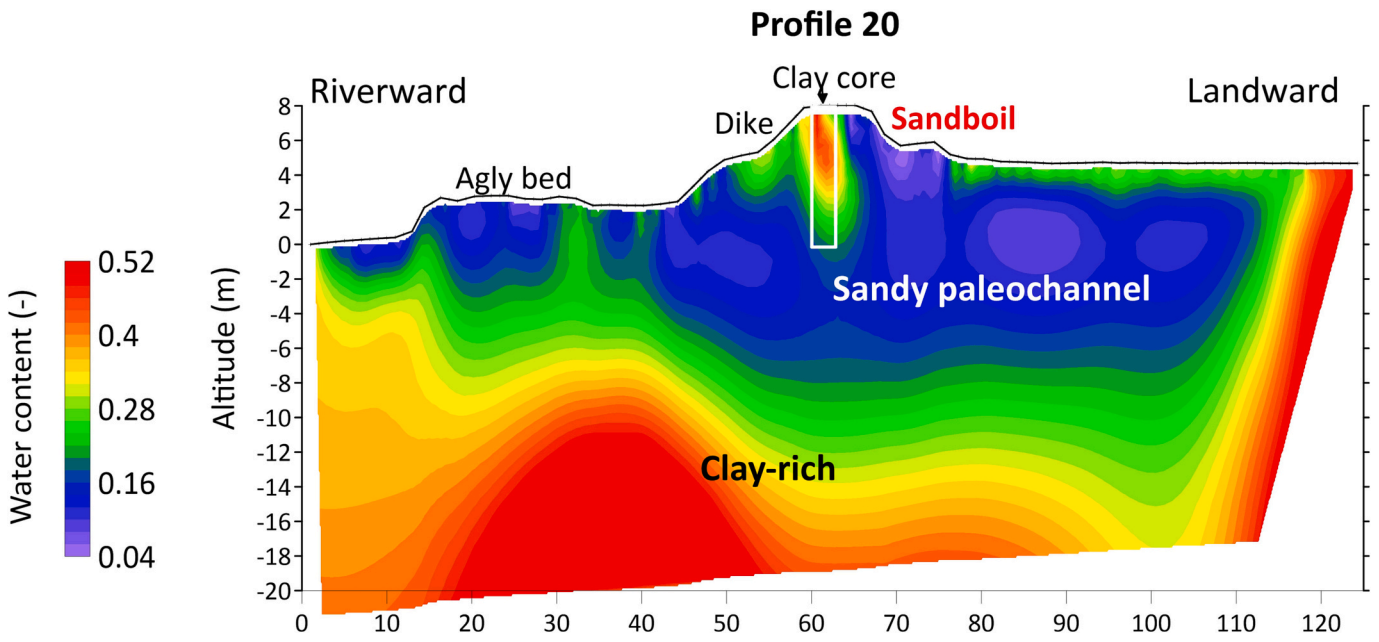

Fig. 14. Water content tomogram of Profile 20 (see position in Fig. 2). We can observe the clay core in the river dike. The depth of the paleochannel is roughly 8 m. We observe that the clay core extends down to the level of the river bed. Trenches and wells in the area show a sand loam body overlying a silt clay material, therefore in agreement with our observations.

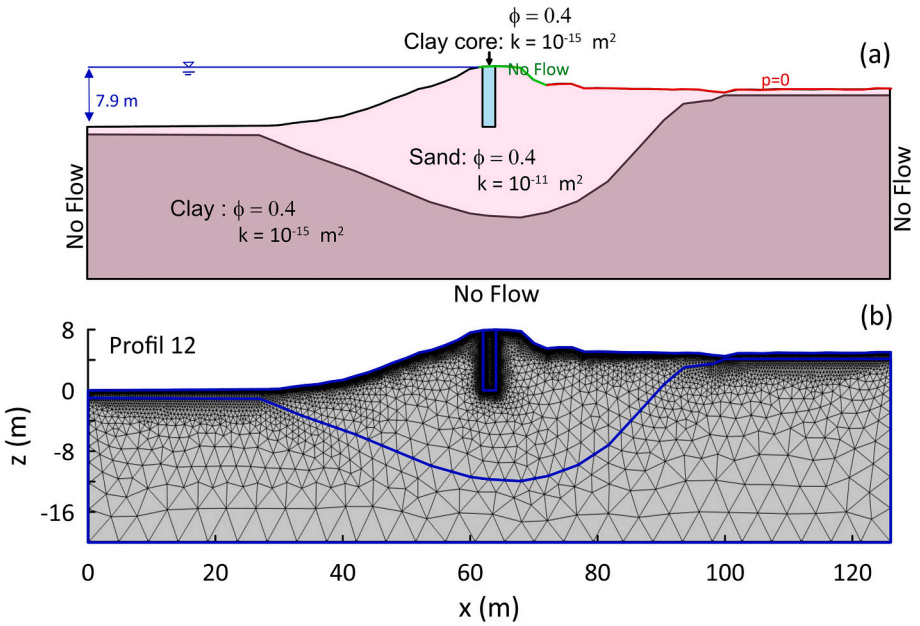

Fig. 15. Numerical hydrogeological simulation along Profile 12. **a.** We use the geometry from Profile 12 (see Fig. 2) to setup the model. We use no flow conditions on the left and right sides, no flow condition on the bottom side. The head is imposed in the river bed riverward with respect to the river dike and an open flow condition on landward. The parameters ϕ and k denote the porosity and the permeability, respectively. Note that the computations are independent of the value of the porosity, which is required only to get the mean pore water velocity through the Dupuit equation. The no-flow condition at the top of the river dike corresponds to the position of the impervious geotextile. **b.** Mesh used for the simulation using the finite element method with Comsol Multiphysics (v.6).

Figs. 10 to 14 show five examples of 2.5D tomograms of the water content determined from the induced polarization survey. We can observe a clay core just below the top of the dike and typically extending down to the river bed level. We knew about the existence of the clay core emplaced to a depth corresponding to the altitude of the river bed. The paleochannel is located below the river dike and constitutes, during flooding conditions, a preferential flow path leading to ground water discharges in the inland side of the dike. The paleochannel broadens further southeast and is less deep. The water content in the paleochannel is small because the survey was carried out during a drought (Spring 2023). In water flooding conditions, the water content in the channel is likely to be much higher. In the next section, we use one of these profiles (Profile 12) to conduct a hydraulic modeling to understand the pattern of discharge in the landside of the dike.

4. Numerical modeling

In this section, our goal is to compute the pattern of ground water

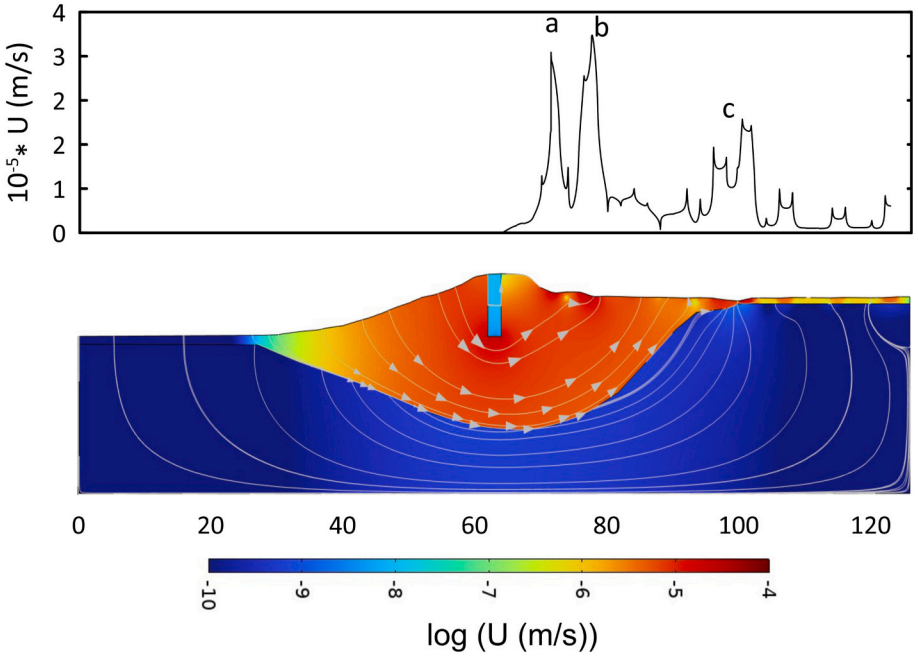

Fig. 16. Numerical hydrogeological simulation of the ground water flow in steady-state conditions and for saturated conditions. Note the three areas (labeled a, b, and c) of water discharges landside the river dike. The discharges a and b are located at the toe of the dike.

flow discharge when the Agly River level is close to over-flooding. We want to see the preferential paths (if any) of the ground water discharge when the permeabilities of the sandy paleochannel and background are taken constant (homogeneous case). In these conditions, the flow of the ground water is purely controlled by the topography and the geometry of the paleochannel. We will not look at the case of solitary or shock waves even if the conditions could be met in the present situation to create such disturbances. Indeed, when the change of fluid pressure in the river is sudden, porosity waves could be created in the sandy paleochannel because permeability has a strong dependence with the fluid pressure itself and he classical Darcy-law degenerates into a Burgers equation admitting shock waves as solution (e.g., Revil and Cathles, 2002). This can yield the formation of mud volcanoes (Revil, 2002).

We use therefore the geometry shown in Fig. 15 with the specific boundary condition (1) no-flow condition on the two sides and bottom side, (2) imposed head over the river bed with a water level close to the top of the dike, and (3) an open boundary on the downstream side of the side to let the ground water discharging through the topography. The ground water flow problem is solved here in saturated conditions (Darcy flow problem):

$$\mathbf{u} = -\frac{k}{\eta_w}\nabla p, \tag{3}$$

$$\nabla\cdot\mathbf{u} = 0. \tag{4}$$

Eq. (3) corresponds to the constitutive equation, i.e., the Darcy's equation for the hydraulic flux vector called the Darcy velocity $\mathbf{u}$ (m s^{-1}), k (in m^2) is the permeability, and η_w denotes the dynamic viscosity of the ground water ($\sim 10^{-3}$ Pa s). Eq. (4) corresponds to the continuity equation (mass conservation equation for the pore water) written here in steady-state condition. The Darcy velocity is therefore conservative. The relationship between the fluid pressure p (in Pa) and the head h (in m) is $p = \rho_w g h$ where $g = 9.81$ m^2 s^{-1} denotes the acceleration of the gravity field and ρ_w denotes the mass density of water (1000 kg m^{-3}). The case we look at is therefore the case of high water levels (river flood) maintained for a relatively long time.

We use a permeability of 10^{-11} m^2 for the sand loam (hydraulic conductivity of $\sim 10^{-4}$ m s^{-1}) and a permeability of 10^{-15} m^2 (hydraulic conductivity of $\sim 10^{-8}$ m s^{-1}) for the silty clay (hydraulic conductivities measured on core samples are in the range 2×10^{-5} m s^{-1} to 3×10^{-9} m s^{-1}). The ground water flow solution is calculated using the finite element method using Comsol Multiphysics (v.6).

The ground water flow solution in terms of Darcy velocity distribution is shown in Fig. 16. We see that the discharge is heterogeneous with three areas of specific discharges. The first discharges *a* and *b* (see Fig. 16) are located at the toe of the dike, precisely where small-scale collapses are noticed. The second discharge *c* (see Fig. 16) is located close to the bank of the paleochannel close to an area marked by some subsidence and sand-boils. This heterogeneous discharge is therefore not controlled by local heterogeneities in the permeability distribution but by the geometry of the problem (topography and geometry of the bottom side of the paleochannel) at the scale of the dike. The mean ground water velocity can be determined from the Darcy velocity divided by the connected porosity (Dupuit equation). This yields ground water discharges with a mean pore velocity of $\sim 10^{-2}$ -10^{-3} cm s^{-1}, which is sufficient to fluidize a sandy material with a density of around 2600 kg. m^{-3} and an average particles diameter of around 350 μm (Amin et al., 2021). Robbins et al. (2019) reported a water velocity on the order of 10 cm s^{-1} for the Mayersville sand boil (Mississipi, USA) which may potentially involve coarser material.

That said if some localized flow persists long enough over time and because of the removal of grains, increasing permeability and reducing flow length over time, and creating the conditions for backward erosion and piping. Such erosion channels may progress under the river dike. Sellmeijer (1989) describes the underlying physics behind erosion processes responsible for piping due to too large vertical hydraulic gradients below the clay core corresponding to the hydraulic barrier placed at the inside toe of the dike (see also Van Beek et al., 2012). We let this type of simulation for the future.

5. Conclusions

We performed 2.5D and 3D resistivity and normalized chargeability tomography over a portion of a river dike of the Agly River in the South-West of France in an area exhibiting fluidization pathologies during flooding events. The tomograms show that in this area, the dike is

located above a paleochannel of the river. The tomograms are interpreted using a petrophysical model known as the dynamic Stern layer model. They are used to map the water content and cation exchange capacity of the subsurface. Geophysical data indicate that the paleochannel is filled with sand and is incised into a clayey bed.

Numerical modeling is used to simulate the hydraulic regime during river floods. The numerical model solves the Darcy flow problem. When the water level is high above the riverbed, groundwater flows across the dike through the permeable paleochannel and under the clayey core of the dike. On the downstream side, the flow is heterogeneous and marked by highly localized flow. The emergence of these preferential flow paths is purely controlled by the topography and geometry of the paleochannel. Further work is needed to better understand the backward erosion and fluidization associated with these localized flow paths. Modeling needs to be carried out to assess the possibility of dike subsidence associated with internal erosion, followed by dike erosion during floods due to water leakage in these areas.

CRediT authorship contribution statement

A. Ghorbani: Writing – review & editing, Writing – original draft, Visualization, Validation, Methodology, Investigation, Formal analysis, Conceptualization. **A. Revil:** Writing – review & editing, Writing – original draft, Visualization, Validation, Resources, Methodology, Investigation, Formal analysis, Data curation, Conceptualization. **S. Bonelli:** Writing – original draft, Visualization, Software, Resources, Project administration, Funding acquisition, Data curation, Conceptualization. **S. Barde-Cabusson:** Writing – review & editing, Writing – original draft, Visualization, Methodology, Investigation, Formal analysis. **L. Girolami:** Writing – review & editing, Writing – original draft, Methodology, Investigation, Funding acquisition, Data curation. **F. Nicoleau:** Writing – review & editing, Project administration, Conceptualization. **P. Vaudelet:** Writing – review & editing, Validation, Funding acquisition, Formal analysis.

Declaration of competing interest

The authors declare that they have no known competing financial interests or personal relationships that could have appeared to influence the work reported in this paper.

Data availability

The data that has been used is confidential.

Acknowledgements

We thank the managers of the river dikes of the Agly River to have let us obtained the authorizations for this work. We thank INRAE, owner of the data, for funding the aerial lidar DTM produced by Sub-C Marine, and for funding the geophysical survey. This work was able to be carried out thanks to the results of the ALCOTRA project RITA funded by the European Community. We thank N. Chaouch (INRAE) and G. Parcillié (NAGA) for their help. We thank the Editor Janusz Wasowski and the two Referees for their time and professional handling and comments, respectively.

References

Abdulsamad, F., Revil, A., Soueid, Ahmed A., Coperey, A., Karaoulis, M., Nicaise, S., Peyras, L., 2019. Induced polarization tomography applied to the detection and the monitoring of leaks in embankments dams and dikes. Eng. Geol. 254, 89–101. https://doi.org/10.1016/j.enggeo.2019.04.001.

Abdulsamad, F., Chitimbo, T., Revil, A., Prime, N., Plé, O., 2023. Imaging the water content of rammed earth materials with induced polarization. Eng. Geol. 322, 107182 https://doi.org/10.1016/j.enggeo.2023.107182.

Aloisi, G., Drews, M., Wallmann, K., Bohrmann, G., 2004. Fluid expulsion from the Dvurechenskii mud volcano (Black Sea) - part I. Fluid sources and relevance to Li, B, Sr, I and dissolved inorganic nitrogen cycles. Earth Planet. Sci. Lett. 225, 347–363. https://doi.org/10.1016/j.epsl.2004.07.006.

Amin, A., Girolami, L., Risso, F., 2021. On the fluidization/sedimentation velocity of a homogeneous suspension in a low-inertia fluid. Powder Technol. 391, 1. https://doi.org/10.1016/j.powtec.2021.05.073.

Antoine, R., Fauchard, C., Fargier, Y., Durand, E., 2015. Detection of leakage areas in an earth embankment from GPR measurements and permeability logging. Int. J. Geophys. 9 https://doi.org/10.1155/2015/610172.

Archie, G.E., 1942. The Electrical Resistivity Log as an Aid in Determining Some Reservoir Characteristics: Petroleum Transactions of AIME, 146, pp. 54–62. https://doi.org/10.2118/942054-G.

Binley, A., Hubbard, S.S., Huisman, J.A., Revil, A., Robinson, D.A., Singha, K., Slater, L. D., 2015. The emergence of hydrogeophysics for improved understanding of subsurface processes over multiple scales. Water Resour. Res. 51, 3837–3866. https://doi.org/10.1002/2015WR017016.

Bolève, A., Crespy, A., Revil, A., Janod, F., Mattiuzzo, J.L., 2007. Streaming potentials of granular media: Influence of the Dukhin and Reynolds numbers. J. Geophys. Res. 112 (B8) https://doi.org/10.1029/2006JB004673.

Bolève, A., Revil, A., Janod, F., Mattiuzzo, J.L., Fry, J.J., 2009. Preferential fluid flow pathways in embankment dams imaged by self-potential tomography. Near Surf. Geophys. 7 (5–6), 447–462. https://doi.org/10.3997/1873-0604.2009012.

Bonelli, S. (Ed.), 2012. Erosion of Geomaterials, Wiley-ISTE.

Bonelli, S. (Ed.), 2013. Erosion in Geomechanics Applied to Dams and Levees, Wiley-ISTE. https://doi.org/10.1002/9781118577165.

Cardarelli, E., Cercato, M., De Donno, G., 2014. Characterization of an earth-filled dam through the combined use of electrical resistivity tomography, P- and SH-wave seismic tomography and surface wave data. J. Appl. Geophys. 106, 87–95. https://doi.org/10.1016/j.jappgeo.2014.04.007.

Carozza, J.M., Puig, C., Odiot, T., Passarrius, O., Valette, P., 2013. L'édification de la basse plaine de la Salanque (Roussillon, France) au cours de la seconde partie de l'Holocène et ses implications sur la répartition des sites archéologiques. Quaternaire. https://doi.org/10.4000/quaternaire.6552, 24/2/2013.

Carter, D.L., Heilman, M.D., Gonzalez, C.L., 1965. Ethylene glycol monoethylether for determining surface area of silicate minerals. Soil Sci. 100 (5), 356–360.

Chew, W., Sen, P., 1982a. Potential of a sphere in an ionic solution in thin double layer approximations.The. J. Chem. Phys. 77 (4), 2042–2044. https://doi.org/10.1063/1.444060.

Chew, W., Sen, P., 1982b. Dielectric enhancement due to electrochemical double layer: thin double layer approximation. J. Chem. Phys. 77 (9), 4683–4693. https://doi.org/10.1063/1.444427.

de Lima, O.A., Sharma, M.M., 1992. A generalized Maxwell-Wagner theory for membrane polarization in shaly sands. Geophysics 57 (3), 431–440. https://doi.org/10.1190/1.1443257.

Duvillard, P.A., Revil, A., Soueid, Ahmed A., Qi, Y., Coperey, A., Ravanel, L., 2018. Three-dimensional electrical conductivity and induced polarization tomography of a rock glacier. J. Geophys. Res. 123 https://doi.org/10.1029/2018JB015965.

El Alam, J., Revil, A.J., Dick, P., 2023. Influence of the water content on the complex conductivity of bentonite. Eng. Geol. 322, 107183 https://doi.org/10.1016/j.enggeo.2023.107183.

Fargier, Y., Lopes, P.S., Fauchard, C., François, D., Côte, P., 2014. DC-Electrical Resistivity Imaging for embankment dike Investigation: a 3D extended normalization approach. J. Appl. Geophys. 103, 245–256. https://doi.org/10.1016/j.jappgeo.2014.02.007.

Fell, R., MacGregor, P., Stapledon, D., 1992. Geotechnical Engineering of Embankment Dams. Balkema, Rotterdam (ISBN 9054101288).

Fell, R., Wan, C.F., Cyganiewicz, J., Foster, M., 2003. Time for development of internal erosion and piping in embankment dams. J. Geotech. Geoenviron. Eng. 127, 307–314. https://doi.org/10.1061/(ASCE)1090-0241(2003)129:4(307).

Fleury, P., Cherlier, J.-B., Bessiere, H., 2020. Caractérisation des crues karstiques sur le basin versant de l'Agly. Rapport Final (BRGM/RP-69551-FR, 176 pp).

Ghorbani, A., Revil, A., Coperey, A., Soueid Ahmed, A., Roque, S., Heap, M.J., Grandis, H., Viveiros, F., 2018. Complex conductivity of volcanic rocks and the geophysical mapping of alteration in volcanoes. J. Volcanol. Geotherm. Res. 357, 106–127. https://doi.org/10.1016/j.jvolgeores.2018.04.014.

Günther, T., Martin, T., 2016. Spectral two-dimensional inversion of frequency-domain induced polarization data from a mining slag heap. J. Appl. Geophys. 135, 436–448. https://doi.org/10.1016/j.jappgeo.2016.01.008.

Hauck, C., 2002. Frozen ground monitoring using DC resistivity tomography. Geophys. Res. Lett. 29, 10–13. https://doi.org/10.1029/2002GL014995.

Himi, H., Casado, I., Sendros, A., Loveraa, L.R., Rivero, L., Casasa, A., 2018. Assessing preferential seepage and monitoring mortar injection through an earthen dam settled over a gypsiferous substrate using combined geophysical methods. Eng. Geol. 246, 212–221. https://doi.org/10.1016/j.enggeo.2018.10.002.

Ingeman-Nielsen, T., 2006. The effect of electrode contact resistance and capacitive coupling on complex resistivity measurements. In: SEG Technical Program Expanded Abstracts, pp. 1376–1380. https://doi.org/10.1190/1.2369776.

Johansson, S., Dahlin, T., 1996. Seepage monitoring in an Earth embankment dam by repeated resistivity measurements. Eur. J. Eng. Environ. Geophys. 1 (3), 229–247.

Jougnot, D., Ghorbani, A., Revil, A., Leroy, P., Cosenza, P., 2010. Spectral Induced Polarization of partially saturated clay-rocks: a mechanistic approach. Geophys. J. Int. 180 (1), 210–224. https://doi.org/10.1111/j.1365-246X.2009.04426.x.

Maurin, J., Ledoux, P., 2013. Retour d'expérience de la crue de l'Agly du 6 mars 2013 mettant en cause des digues de classe A. Rapport 37. https://www.researchgate.net/publication/259574923_Retour_d'experience_de_la_crue_de_l'Agly_du_6_mars_2013.

Niu, Q., Revil, A., Saidian, M., 2016. Salinity dependence of the complex surface conductivity of the Portland sandstone. Geophysics 81 (2), D125–D140. https://doi.org/10.1190/GEO2015-0426.1.

Nordsiek, S., Diamantopoulos, E., Hördt, A., Durner, W., 2015. Relationships between soil hydraulic parameters and induced polarization spectra. Near Surf. Geophys. 14, 23–37. https://doi.org/10.3997/1873-0604.2015048.

Okay, G., Leroy, P., Ghorbani, A., Cosenza, P., Camerlynck, C., Cabrera, J., Florsch, N., Revil, A., 2014. Spectral induced polarization of clay-sand mixtures. Experiments and modelling. Geophysics 79 (6), E353–E375. https://doi.org/10.1190/GEO2013-0347.1.

Panthulu, T.V., Krishnaiah, C., Shirke, J.M., 2001. Detection of seepage paths in earth dams using self-potential and electrical resistivity methods. Eng. Geol. 59 (3–4), 281–295. https://doi.org/10.1016/S0013-7952(00)00082-X.

Perri, M.T., Boaga, J., Bersan, S., Cassiani, G., Cola, S., Deiana, R., Simonini, P., Patti, S., 2014. River embankment characterization: the joint use of geophysical and geotechnical techniques. J. Appl. Geophys. 11, 5–22. https://doi.org/10.1016/j.jappgeo.2014.08.012.

Revil, A., 2002. Genesis of mud volcanoes in sedimentary basins. A solitary wave-based mechanism. Geophys. Res. Lett. 29 (12), 1574. https://doi.org/10.1029/2001GL014465.

Revil, A., 2013a. Effective conductivity and permittivity of unsaturated porous materials in the frequency range 1mHz-1GHz. Water Resour. Res. 49, 306–327. https://doi.org/10.1029/2012WR012700.

Revil, A., 2013b. On charge accumulations in heterogeneous porous materials under the influence of an electrical field. Geophysics 78 (4), D271–D291. https://doi.org/10.1190/GEO2012-0503.1.

Revil, A., Cathles, L.M., 2002. Fluid transport by solitary waves along growing faults: a field example from the South Eugene Island Basin, Gulf of Mexico. Earth Planet. Sci. Lett. 202 (2), 321–335 (erratum: Revil, A. and L.M., Cathles, Fluid transport by solitary waves along growing faults: a field example from the South Eugene Island Basin, Gulf of Mexico, Earth and Planetary Science letters, 204(1-2), 321-322, 2002).

Revil, A., Florsch, N., 2010. Determination of permeability from spectral induced polarization in granular media. Geophys. J. Int. 181 (3), 1480–1498. https://doi.org/10.1111/j.1365-246X.2010.04573.x.

Revil, A., Cary, L., Fan, Q., Finizola, A., Trolard, F., 2005. Self-potential signals associated with preferential ground water flow pathways in a buried paleo-channel. Geophys. Res. Lett. 32, L07401. https://doi.org/10.1029/2004GL022124.

Revil, A., Eppehimer, J.D., Skold, M., Karaoulis, M., Godinez, L., Prasad, M., 2013. Low-frequency complex conductivity of sandy and clayey materials. J. Colloid Interface Sci. 398, 193–209. https://doi.org/10.1016/j.jcis.2013.01.015.

Revil, A., Florsch, N., Camerlynck, C., 2014. Spectral induced polarization porosimetry. Geophys. J. Int. 198, 1016–1033. https://doi.org/10.1093/gji/ggu180.

Revil, A., Coperey A., Shao Z., Florsch N., Fabricius I. L., Deng Y., Delsman J.R, Pauw P. S., Karaoulis M., de Louw P. G. B., van Baaren E. S., Dabekaussen W., Menkovic A., Gunnink J. L., 2017. Complex conductivity of soils. Water Resour. Res., 53, 8, 7121–7147. doi: https://doi.org/10.1002/2017WR020655.

Revil, A., Soueid, Ahmed A., Coperey, A., Ravanel, L., Sharma, R., Panwar, N., 2020. Induced polarization as a tool to characterize shallow landslides. J. Hydrol. 589, 125369 https://doi.org/10.1016/j.jhydrol.2020.125369.

Robbins, B.A., Van Beek, V.M., 2015. Backward erosion piping: A historical review and discussion of influential factors. In: Association of State dam Safety Officials Annual Conference 2015 (Dam Safety 2015), vol. 2. Association of State Dam Safety Officials, Lexington, KY, USA, pp. 919–938.

Robbins, B.A., Stephens, I.J., Van Beek, V.M., Koelewijn, A.R., Bezuijen, A., 2019. Field measurements of sand boil hydraulics. Géotechnique 1. https://doi.org/10.1680/jgeot.18.P.151, 8 pp.

Schlumberger, C., 1920. Etude Sur la Prospection Électrique du sous-sol, Gauthier-Villars, Paris. The second edition without modification is available at. https://gallica.bnf.fr/ark:/12148/bpt6k64569898.texteImage. English version, translated by Sherwin F. Kelly: "Study of underground electrical prospection". Available at: https://archive.org/details/studyofundergrou00schlrich/page/n37.

Sellmeijer, J.B., 1989. On the Mechanism of Piping under Impervious Structures (Ph-D thesis TU-Delft).

Soueid Ahmed, A., Revil, A., Jardani, A., Chen, R., 2018. Geostatistical inversion of induced polarization data and its application to coal seam fires. Geophysics 83 (3), E133–E150. https://doi.org/10.1190/geo2017-0232.1.

Stephens, I.J., 2014. Field Investigation of a Sand Boil Developed during the Mississippi River Flood of 2011, *Dam Safety 2014 Proceedings of the Association of State dam Safety Officials 31st Annual Conference,* Sep 21–25, San Diego, CA.

Titov, K., Komarov, V., Tarasov, V., Levitski, A., 2002. Theoretical and experimental study of time domain-induced polarization in water-saturated sands. J. Appl. Geophys. 50, 417–433. https://doi.org/10.1016/S0926-9851(02)00168-4.

Van Beek, V., Yao, Q., Van, M., Barends, F., 2012. Validation of Sellmeijer's model for backward piping under dikes on multiple sand layers. In: Proc. 6th Int. Conf. On Scour and Erosion, Paris, France, pp. 543–550.

Van Beek, V., Van Essen, H., Vandenboer, K., Bezuijen, A., 2015. Developments in modelling of backward erosion piping. Geotechnique 65 (9), 740–754. https://doi.org/10.1680/geot.14.P.119.

Vaudelet, P., Revil, A., Schmutz, M., Franceschi, M., Bégassat, P., 2011. Induced polarization signature of the presence of copper in saturated sands. Water Resour. Res. 47, W02526. https://doi.org/10.1029/2010WR009310.

Vinegar, H., Waxman, M., 1984. Induced polarization of shaly sands. Geophysics 49 (8), 1267–1287. https://doi.org/10.1190/1.1441755.

Wagner, F.M., Mollaret, C., Kemna, A., Hauck, C., 2019. Quantitative imaging of water, ice and air in permafrost systems 1210 through petrophysical joint inversion of seismic refraction and electrical resistivity data. Geophys. J. Int. 219, 1866–1875. https://doi.org/10.1093/gji/ggz402.

Waxman, M.H., Smits, L.J.M., 1968. Electrical conductivities in oil-bearing shaly sands. Soc. Pet. Eng. J. 8 (2), 107–122. https://doi.org/10.2118/1863-A.

Weller, A., Slater, L., Nordsiek, S., 2013. On the relationship between induced polarization and surface conductivity: Implications for petrophysical interpretation of electrical measurements. Geophysics 78 (5), D315–D325. https://doi.org/10.1190/geo2013-0076.1.

Zimmermann, E., Kemna, A., Berwix, J., Glaas, W., Münch, H.M., Huisman, J.A., 2008. A high-accuracy impedance spectrometer for measuring sediments with low polarizability. Meas. Sci. Technol. 19 (10), 105603 https://doi.org/10.1088/0957-0233/19/10/105603.

Zisser, N., Nover, G., 2009. Anisotropy of permeability and complex resistivity of tight sandstones subjected to hydrostatic pressure. J. Appl. Geophys. 68, 356–370. https://doi.org/10.1016/j.jappgeo.2009.02.010.

Zisser, N., Kemna, A., Nover, G., 2010. Relationship between low-frequency electrical properties and hydraulic permeability of low-permeability sandstones. Geophysics 75 (3), E131–E141. https://doi.org/10.1190/1.3413260.

Zukoski, C.F., Saville, D.A., 1986a. The interpretation of electrokinetic measurements using a dynamic model of the Stern layer: I, the dynamic model. J. Colloid Interface Sci. 114 (1), 32–44. https://doi.org/10.1016/0021-9797(86)90238-9.

Zukoski, C.F., Saville, D.A., 1986b. The Interpretation of electrokinetic measurements using a dynamic model of the Stern layer: II, comparisons between theory and experiments. J. Colloid Interface Sci. 114 (1), 45–53. https://doi.org/10.1016/0021-9797(86)90239-0.